Plasma Chemistry and Plasma Processing (2024) 44:2101–2118
https://doi.org/10.1007/s11090-024-10501-8

RESEARCH

Reaction Pathways and Energy Consumption in NH_3 Decomposition for H_2 Production by Low Temperature, Atmospheric Pressure Plasma

Brian N. Bayer[1] · Aditya Bhan[1] · Peter J. Bruggeman[2]

Received: 27 July 2024 / Accepted: 16 August 2024 / Published online: 28 August 2024

Abstract

Pathways for NH_3 decomposition to N_2 and N_2H_4 by atmospheric pressure nonthermal plasma are analyzed using a combination of molecular beam mass spectrometry measurements and zero-dimensional kinetic modeling. Experimental measurements show that NH_3 conversion and selectivity towards N_2 formation scale monotonically with the specific energy input into the plasma with ~ 100% selectivity to N_2 formation achieved at specific energy inputs above 0.12 J cm^{-3} (3.1 eV (molecule NH_3)$^{-1}$). The kinetic model recovers these trends, although it underpredicts N_2 selectivity at low specific energy input. These discrepancies can be explained by the underestimation of reaction rate coefficients for reactions that consume N_2H_x species in collisions with H radicals and/or radial nonuniformities in power deposition, gas temperature, and species concentrations that are not represented by the plug flow approximation used in the model. The kinetic model shows that N_2 formation proceeds through N_2H_x decomposition pathways rather than NH_x decomposition pathways in low temperature, atmospheric pressure plasma. Higher selectivity toward N_2 production can be achieved by operating at higher NH_3 conversion and with a higher gas temperature. The high energy cost of NH_3 decomposition by atmospheric pressure nonthermal plasma found in this work (25–50 eV (molecule NH_3 converted)$^{-1}$; 17–33 eV (molecule H_2 formed)$^{-1}$) is a result of the energy requirement for electron-impact dissociation of NH_3 and the significant re-formation of NH_3 by three-body recombination reactions between NH_2 and H.

Keywords Nonthermal plasma · Ammonia decomposition · Molecular beam mass spectrometry · Kinetic modeling

✉ Aditya Bhan
abhan@umn.edu

✉ Peter J. Bruggeman
pbruggem@umn.edu

[1] Department of Chemical Engineering and Materials Science, University of Minnesota-Twin Cities, 421 Washington Ave. SE, Minneapolis, MN 55455, USA

[2] Department of Mechanical Engineering, University of Minnesota-Twin Cities, 111 Church St. SE, Minneapolis, MN 55455, USA

Introduction

NH_3 can potentially serve as a platform molecule to store renewable energy in a medium that can be easily stored and transported [1]. However, before energy conversion by combustion or in fuel cells, NH_3 must be partially or fully decomposed into N_2 and H_2 because NH_3 has a low flammability, is difficult to ignite, and NH_3 fuel cell technology is less developed than H_2 fuel cell technology [2]. NH_3 decomposition to N_2 and H_2 is an endothermic reaction with a positive entropy of reaction ($\Delta H = 46$ kJ (mol NH_3)$^{-1}$ = 0.48 eV (molecule NH_3)$^{-1}$; $\Delta S = 99$ J (mol NH_3)$^{-1}$ K^{-1}) [3]. To operate at process conditions that favor NH_3 decomposition, gas-phase NH_3 pyrolysis typically occurs at temperatures above 1000 K [4]. Heterogeneous catalysts can be utilized to lower operating temperatures for NH_3 decomposition to ~ 700 K; however, currently the most effective catalysts are expensive noble metals (Ru) [5]. NH_3 decomposition can be carried out catalytically at lower temperatures by oxidative reforming processes, although this method sacrifices some H_2 to form H_2O to make the overall reaction more exothermic [5].

Nonthermal plasma provides an opportunity to drive NH_3 decomposition at low temperatures utilizing high-energy electrons to excite or dissociate N–H bonds in NH_3. Qiu et al. [6], Gao et al. [7], and Ruiz-Martín et al. [8] demonstrate that atmospheric pressure, nonthermal plasma can drive NH_3 decomposition in Ar/NH_3 or pure NH_3 discharges without external heating, indicating that the plasma can drive NH_3 decomposition via nonthermal processes or in-situ heating. Kinetic models to describe NH_3 decomposition in Ar/NH_3 microdischarges at 100 torr developed by Arakoni et al. [9] show that > 95% of NH_3 dissociation is induced by electron impact processes at select process conditions, indicating that NH_3 decomposition can be driven by nonthermal processes. They also investigated how changing operating conditions can optimize the energy cost of H_2 production, noting an optimal energy cost of H_2 production equal to 3.3 eV (molecule H_2 consumed)$^{-1}$. They, as well as Qiu et al. [6], note that this energy cost is higher than the heat of combustion of H_2 (− 2.5 eV (molecule H_2 consumed)$^{-1}$ [3]), which is the amount of energy that can be recovered from H_2 oxidation in a fuel cell. These studies do not, however, analyze the chemical or physical processes that dictate the energy cost in order to identify methods to lower the energy cost of the plasma-driven NH_3 decomposition.

N_2 and H_2 are not the only products that can form from NH_3 decomposition. Fateev et al. [10] note that N_2H_4 (hydrazine), a toxic compound and a strong reductant [11], was a side product of NH_3 decomposition in an Ar/NH_3 DBD at 300 K. They posit that N_2H_4 was formed from three-body collisions between NH_2 radicals but do not perform extensive experiments or kinetic modeling to validate this claim. Bang et al. [12] investigated possible mechanisms for NH_3 decomposition in a 1% NH_3 / 99% N_2 atmospheric pressure dielectric barrier discharge using a combination of experimental measurements and kinetic modeling. According to their proposed reaction mechanism, N_2H_4 is formed from three-body collisions between NH_2 radicals, although they do not measure N_2H_4 in their experiments to help validate their proposed reaction pathways. Their mechanism shows that N_2H_4 may be an intermediate in NH_3 decomposition but that NH_3 decomposition can also proceed through NH_x decomposition pathways mediated by the presence of N_2-derived species in their plasma.

This work utilizes a combination of molecular beam mass spectrometry and zero-dimensional kinetic modeling to assess energy consumption and reaction pathways involved in NH_3 decomposition and formation of N_2 and N_2H_4 in an RF-driven atmospheric pressure plasma jet. Experimental measurements show that NH_3 conversion and selectivity towards

N_2 formation increases with the specific energy input into the system. Kinetic modeling results recover these trends but underpredict selectivity toward N_2. These underpredictions can be resolved by considering potential inaccuracies associated with reaction rate constants and/or radial nonuniformities in power deposition, gas temperature, and species concentrations that cannot be described with a plug-flow approximation. Results of the kinetic model demonstrate that N_2H_4 is an intermediate in N_2 formation from NH_3 decomposition at atmospheric pressure. N_2H_4 production can be mitigated by operating the plasma jet at higher NH_3 conversion and higher gas temperature. The kinetic model demonstrates that NH_3 dissociation is induced by electron impact dissociation, which has an energy threshold of 5.72 eV [13]. This gives a lower bound on energy cost for H_2 production to be 3.8 eV (molecule H_2 produced)$^{-1}$ if electron impact dissociation is the dominant method of NH_3 dissociation. This value is higher than the heat of combustion of H_2, indicating that plasma-driven NH_3 decomposition via solely electron impact dissociation processes would cost too much energy to be utilized to produce H_2 for energy storage applications. Recombination reactions between NH_2 and H to form NH_3 further increase the energy cost of low temperature plasma-driven NH_3 decomposition at atmospheric pressure.

Methods

Plasma Jet and MBMS Setup

An RF-driven (13.8 MHz) atmospheric pressure plasma jet with a feed gas containing mixtures of 5% NH_3 in Ar (Airgas), N_2 (HP, Airgas, 99.998% purity), 4% H_2 in Ar (HP, Airgas, 99.995% purity), and Ar (UPC, Airgas, 99.9993% purity) at total flow rates ranging from 0.5 to 6.0 standard liters per minute (slm) was utilized in this work (Fig. 1). The jet consisted of a 3 mm outer diameter, 2 mm inner diameter quartz tube with two electrodes: an inner 1 mm diameter tungsten needle electrode and an outer copper ring electrode (5.5 mm long), with the tip of the needle in the center of the ground electrode [14]. The distance between the end of the ground electrode and the nozzle of the plasma jet was kept at 10 mm throughout this work. The sampling plate of the mass spectrometer was placed adjacent to the nozzle (< 0.2 mm). Methods used for the RF power measurement are described in more detail by Hofmann et al. [15]. The plasma-on power was varied from 2.2 to 4.05 W in this work, with an optional 20 kHz, 50% duty cycle modulation utilized to lower the average

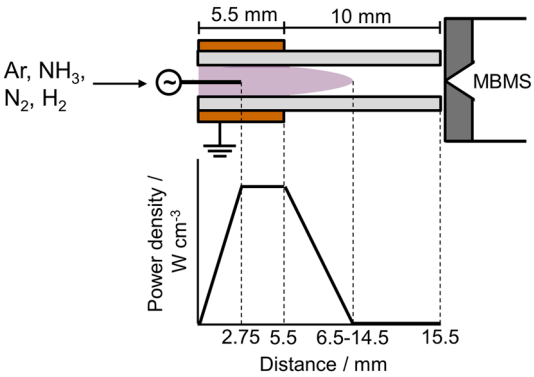

Fig. 1 Experimental setup and power density profile utilized in the kinetic model

power by a factor of two. The waveform was modulated with an additional 10 Hz modulation cycle to enable multi-channel scaler measurements with the MBMS (Sect. "Molecular Beam Mass Spectrometry (MBMS) Methods".).

Molecular Beam Mass Spectrometry (MBMS) Methods

MBMS was utilized in this work to detect and quantify densities of N_2, H_2, NH_3, and N_2H_4. Details about the setup and operation of the MBMS are described in more detail in previous work [16, 17]. Table 1 displays the MBMS methods used in this work to detect and quantify these species. NH_3 was detected at an electron energy of 16 eV to reduce the background signal coming from the dissociative ionization of H_2O ($m_{NH_3^+} = m_{OH^+} = 17$) in the last stage of the MBMS, and N_2H_4 was detected at an electron energy of 15 eV to potentially reduce the background signal coming from the ionization of O_2 ($m_{N_2H_4^+} = m_{O_2^+} = 32$) in the last stage of the MBMS. N_2 was utilized to calibrate N_2H_4 densities due to their similar mass [18]. An additional correction was made when calibrating for N_2H_4 to account for the differences in ionization cross sections between N_2 and N_2H_4 [19]. Attempts to measure the densities of N, H, NH, NH_2, N_2H, N_2H_2/H_2NN, and N_2H_3 were also pursued using methods described in previous work [17]. Densities of these species, aside from possibly N_2H_3, were below the detection limit (~ 10^{13}–10^{14} cm^{-3} for N, NH_x, and N_2H_x; ~ 10^{15} cm^{-3} for H) for the investigated operating conditions [17]. A signal for N_2H_3 (m/z = 31 at 15 eV) could be detected but was consistently smaller than the N_2H_4 signal. It is possible that this signal could arise from dissociative ionization of N_2H_4 in the ionizer of the mass spectrometer, so the detection and enumeration of this species was not investigated in detail in this work.

A multichannel scaler measurement with a plasma modulation at 10 Hz was utilized to quantify changes in the MBMS signal when the plasma was on and off, which can occur due to chemical reactions that consume/form species, vibrational excitation (for N_2) [20, 21], or gas heating if the species is present in the feed gas [22]. For Ar/NH_3 plasmas, H_2 formation (Δc_{H_2}) and N_2H_4 formation ($\Delta c_{N_2H_4}$) were quantified, and NH_3 consumption (Δc_{NH_3}) and N_2 formation (Δc_{N_2}) due to chemical reactions were calculated using H- (Eq. 1) and N- (Eq. 2) atom balances, assuming that N_2, H_2, and N_2H_4 were the only products formed:

$$\Delta c_{NH_3} = -\left(\frac{2}{3}\Delta c_{H_2} + \frac{4}{3}\Delta c_{N_2H_4}\right) \tag{1}$$

$$\Delta c_{NH_3} = -2(\Delta c_{N_2} + \Delta c_{N_2H_4}) \tag{2}$$

This method eliminates confounding effects that gas heating may have on the NH_3 signal and that vibrational excitation may have on the N_2 signal.

Table 1 Summary of detection and calibration methods used for species of interest in this work

Species	m/z	Electron energy / eV	Calibration gas
NH_3	17	16	NH_3
H_2	2	70	H_2
N_2	28	70	N_2
N_2H_4	32	15	N_2

NH_3 fractional conversion (X_{NH_3}) and N_2 selectivity (S_{N_2}) are computed to compare results between experiments and simulations among different process conditions. NH_3 fractional conversion is calculated using Eq. 3:

$$X_{NH_3} = \frac{-\Delta c_{NH_3}}{c_{NH_{3,inlet}} \frac{T_{g,out}}{300K}} \tag{3}$$

In Eq. 3, $c_{NH_{3,inlet}}$ is the concentration of NH_3 at the inlet of the reactor, and $T_{g,out}$ is the gas temperature at the outlet. The $\frac{T_{g,out}}{300K}$ term in Eq. 3 accounts for the decrease in the inlet concentration of NH_3 due to gas heating. $T_{g,out}$ is calculated using Eq. 7 described in Sect. "Zdplaskin Model". N_2 selectivity is calculated using Eq. 4, assuming that N_2 and N_2H_4 are the most abundant nitrogen-containing products of NH_3 decomposition:

$$S_{N_2}[\%] = \frac{\Delta c_{N_2}}{\Delta c_{N_2} + \Delta c_{N_2H_4}} \cdot 100 \tag{4}$$

Zdplaskin Model

A kinetic model was developed using zdplaskin to determine the important pathways and reactions relevant to NH_3 decomposition in the experiments. Zdplaskin [23] concurrently solves species concentration balances, the energy balance for heavy species, and the Boltzmann equation for the electron energy distribution using Bolsig [24]. Electron–electron and electron–ion collisions were not considered when using Bolsig due to the low degree of ionization ($< 10^{-7}$). The inlet gas composition, gas flow rate, inlet gas temperature, pressure, and power deposition profile were used as inputs for the model. A finite but small seed electron density (10^7 cm^{-3}) and reduced electric field (0.001 Td) were used as inlet conditions to initiate the simulations.

The power density profile used in simulations is displayed in Fig. 1 and was assumed to rise from the start of ground electrode to the end of the inner electrode, stay constant from the end of the inner electrode to the end of the ground electrode, and fall from the end of the ground electrode to the end of the plasma plume, which depends on the experimental operating condition (Table S6). Integration of the power density profile over the volume of the reactor yields the experimentally measured power at the corresponding operating condition. For experiments that utilized 20 kHz modulation with a 50% duty cycle, corresponding simulations did not employ power modulation but rather operated with continuous power deposition decreased by a factor of two. This method has been demonstrated to reasonably approximate the effects of power modulation [25]. Power density (P_{dens}) was converted to reduced electric field (E/N; electric field divided by gas density), the input required for zdplaskin, at each timestep using Eq. 5 and Eq. 6:

$$P_{dens} = JE \tag{5}$$

$$J = n_e v_{drift} \tag{6}$$

In Eq. 5 and Eq. 6, J is the current density, E is the electric field strength, n_e is the electron density, and v_{drift} is the electron drift velocity. Zdplaskin calculates the current density by calculating the electron density and drift velocity iteratively at each timestep in the plasma. The model assumes an effective DC electric field in contrast to the RF

field used in experiments. Gas heating due to power deposition was considered in the model using Eq. 7:

$$T_g(\tau) = 300 + \int_0^\tau \frac{RT_g(t)}{pC_{p,\mathrm{Ar}}} P_{dens}(t)dt \tag{7}$$

In Eq. 7, τ is the residence time in the reactor, R is the gas constant, p is the gas pressure (10^5 Pa), $C_{p,\mathrm{Ar}}$ is the heat capacity of Ar at constant pressure [J mol^{-1} K^{-1}], and t is time. This method provides an upper bound on the gas temperature increase through the reactor but is a reasonable estimate because only a small fraction of the energy deposited into the plasma goes into changing the end chemical composition of the system (see Sect. "Assessment of the Energy Efficiency of Plasma-Driven NH_3 Decomposition".) and because gas residence times are short (< 5 ms) so that radial heat transfer away from the plasma jet is insignificant [26]. Outlet gas temperatures are listed in Table S6 for each simulation and range from 313 to 617 K.

Time, the independent variable in zdplaskin, was converted to distance (z) using Eq. 8 by considering the inlet volumetric flow rate (F), the cross sectional area of the reactor (A), and changes in the volumetric gas flow rate due to gas heating.

$$z(\tau) = \int_0^\tau \frac{F}{A(t)} \frac{T_g(t)}{300\ \mathrm{K}} dt \tag{8}$$

The change in volumetric flow rate that would occur due to molar expansion (an increase in molecules due to the stoichiometry of NH_3 decomposition) was neglected due to the high degree of dilution used in this work (99% Ar).

The source code for the reaction set was developed using the reaction set made available by Bang et al. [12]. The reaction set was modified to include reactions involving Ar-derived species and by replacing rate coefficients that were potentially inaccurate. A detailed list of reactions and their rate constants is presented in the supporting information (section S.1.). Electron-impact reactions involving NH_3 and Ar were taken from the Hayashi database, and electron-impact reactions involving N_2 and H_2 were taken from the Lisbon database [13, 27]. Vibrational excitation of N_2, H_2, and NH_3 by electron impact was considered in the model for purposes of determining the electron energy distribution function (EEDF), although concentrations of the vibrationally excited states of these species were assumed to remain at zero in the model. Electron impact reactions involving NH_2, NH, N, and H were not considered because the addition of these reactions caused segmentation faults when trying to run zdplaskin. It is assumed that the inclusion of these reactions would not significantly change the EEDF or concentrations of these species because they accumulate to densities that are smaller than the densities of Ar, N_2, H_2, and NH_3. Reaction rate coefficients for ion recombination reactions, charge transfer reactions, and chemistry related to Ar- and N-based excited states were taken from Bang et al. [12], Arakoni et al. [9], and Van Gaens & Bogaerts [28]. Reaction rate coefficients involving ground state neutral species were mostly taken from the NH_3 pyrolysis mechanism from Alturaifi et al. [29]. As noted by Bang et al. [12], some of the reaction rate coefficients for three-body recombination reactions presented by Alturaifi et al. [29] extrapolate to unrealistic values near 300 K. For these reactions, rate constants were taken from alternative sources [30–33]. Reaction rate coefficients for the reverse reactions of those listed by Alturaifi et al. [29] and alternative sources [30–33] were calculated using the principle of detailed balance with thermodynamic data from

the NIST database [3] for all species aside from N_2H_x species. For N_2H_x species, thermodynamic data was retrieved from the Burcat database [34].

Results

MBMS measurements were performed to assess the influence that power and flow rate have on NH_3 conversion and formation of N_2 and N_2H_4 for 1% NH_3 in Ar plasma (Figure S1). These data were reformulated to plot NH_3 consumption and selectivity towards N_2 formation as a function of specific energy input (SEI, the power divided by the flow rate) as shown in Fig. 2. This figure shows that NH_3 conversion and N_2 selectivity (with N_2H_4 being the other N-containing product) monotonically increase with SEI. The observation that NH_3 fractional conversion increases with SEI is consistent with previous studies of plasma-driven NH_3 decomposition [9].

Increasing the SEI will increase both the electron density and the gas temperature of the plasma. Therefore, the increase in NH_3 fractional conversion and N_2 selectivity with higher SEI can result from nonthermal (electron-driven) and/or thermal (temperature-driven) processes. The correlation between the higher selectivity toward N_2H_4 formation at lower NH_3 conversions also suggests that N_2H_4 could be a primary product of NH_3 decomposition that then reacts further to form N_2. Measurements were made to compare N_2H_4 production in Ar/NH_3 plasma and $Ar/N_2/H_2$ plasma with the same N- and H- content and operating conditions to determine whether N_2H_4 is a product of NH_3 decomposition or is formed from reactions involving plasma-derived N_2/H_2 species (Fig. 3(a)). N_2H_4 formation is measureable in Ar/NH_3 plasma, whereas N_2H_4 formation is below the detection limit in $Ar/N_2/H_2$ plasma, indicating that N_2H_4 is indeed a product of NH_3 decomposition rather than reactions involving plasma-derived N_2/H_2 species. These data also show that the plasma jet induces a greater change in NH_3 density in Ar/NH_3 plasma than in $Ar/N_2/H_2$ plasma by $>20\times$ (Fig. 3(b)). This observation demonstrates that at these investigated operating conditions, the atmospheric pressure RF plasma jet more effectively channels energy towards reactions that decompose NH_3 than reactions that synthesize NH_3.

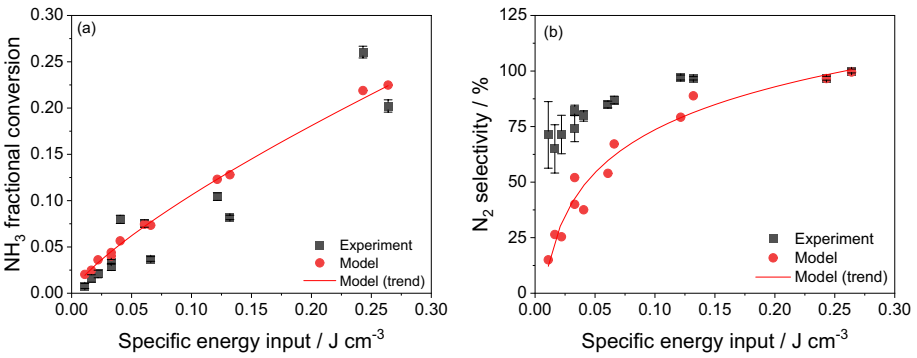

Fig. 2 A comparison between SEI and **a** NH_3 fractional conversion and **b** N_2 selectivity measured in experiments and predicted by kinetic modeling simulations. Experimental conditions: 1% NH_3 in Ar, 0.5–6 slm, 13.8 MHz, 2.2–4.05 W plasma-on power, 10 Hz, 50% duty cycle modulation for MBMS measurements. For the 1.1 W data, the plasma was run with 2.2 W plasma-on power with 20 kHz, 50% duty cycle modulation. Error bars represent 95% confidence intervals. 1 J cm^{-3} = 26 eV (NH_3 molecule) $^{-1}$. The lines in **a** and **b** serve as a guide to the eye to describe the trend of the kinetic modeling simulation results

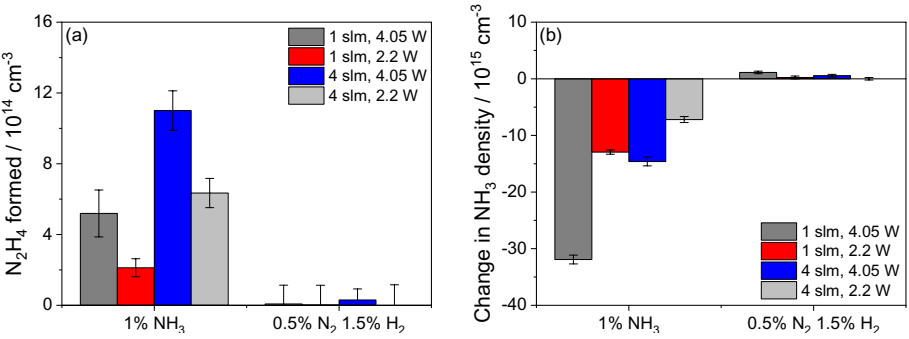

Fig. 3 **a** N_2H_4 formation and **b** changes in NH_3 density in 1% NH_3 in Ar and 0.5% N_2, 1.5% H_2 in Ar plasma. Experimental conditions: 1% NH_3 in Ar, 1–4 slm, 13.8 MHz, 2.2–4.05 W plasma-on power, 10 Hz, 50% duty cycle modulation for MBMS measurements. Error bars represent 95% confidence intervals

To determine which reactions contribute to NH_3 decomposition, N_2H_4 production, and N_2 production, kinetic modeling was performed with the model described in Sect. "Zdplaskin Model". to simulate the process conditions reported in Fig. 2. The results from these simulations are plotted in Fig. 2 alongside the experimental data. The simulations quantitatively agree with the experimental data relating SEI to NH_3 conversion. Though the simulations systematically underestimate N_2 selectivity, especially at lower SEI, they do accurately reproduce the observation that N_2 selectivity increases with SEI.

Axial changes in concentrations of intermediates and reaction rates predicted by the model are analyzed to assess reaction pathways and chemical reactions relevant for NH_3 decomposition and N_2/N_2H_4 formation. Axial variations in power density deposition (as the input, see Sect. "Zdplaskin Model".), electron density, electron temperature, gas temperature, and concentrations of products (N_2H_4, N_2, H_2) and intermediates (N, H, NH, NH_2, N_2H, N_2H_2, H_2NN, N_2H_3) are displayed in Fig. 4. The electron density is proportional to the power deposition profile in the plasma and then decays in the afterglow. The electron temperature in the plasma predicted by the model (~2 eV) is slightly higher and the electron density (~10^{11} cm^{-3}) is lower than what would be expected for atmospheric pressure RF plasma jets, which typically have electron temperatures around 1–2 eV and electron densities ~10^{12}–10^{13} cm^{-3} [15, 35, 36]. This has been previously observed in global models that spatially average plasma parameters and is ascribed to not considering secondary emission from metal electrodes or photoionization as ionization sources in such models [25, 37].

Species density profiles shown in Fig. 4(b) demonstrate that N_2H_4 density peaks in the plasma at around 0.44 cm (650 µs) and then decays simultaneously with a rise in N_2 density, suggesting that N_2H_4 forms over shorter timescales in the plasma and then is consumed to form N_2 over longer timescales. The decrease in NH_3 density exhibited in Fig. 4(b) mostly occurs due to gas rarefaction, since the gas temperature increases from 300 to 448 K due to gas heating (Fig. 4(a)). The data in Fig. 4(c) show that concentrations of N_2H_x species decrease as the degree of hydrogenation decreases, indicating that these species become more unstable as more hydrogen is removed. Axial profiles of NH_2 reported in Fig. 4(d) show that NH_2 concentrations are highest in the plasma but then drop by over two orders of magnitude in < 100 µs in the spatial afterglow of the plasma because of its high reactivity.

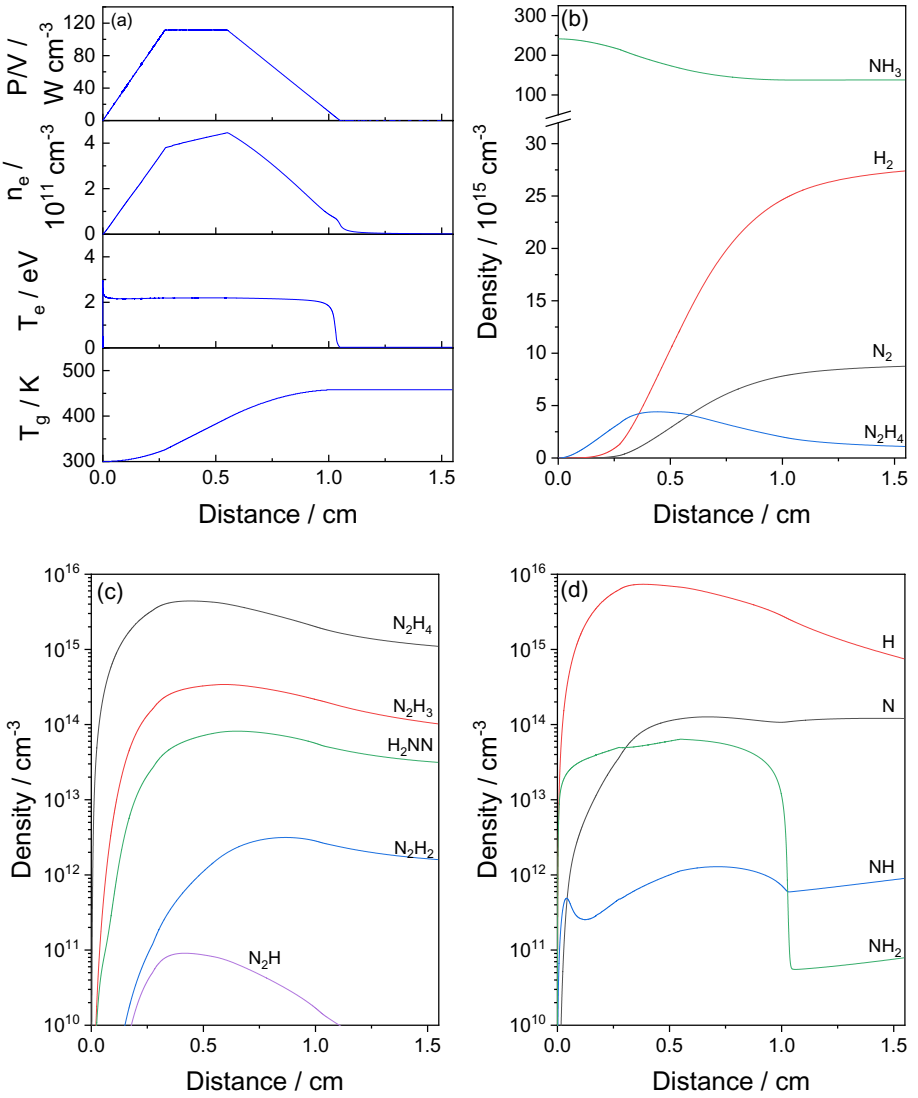

Fig. 4 Axial profiles of **a** power density, electron density, electron temperature, and gas temperature; **b** NH_3, N_2, H_2, and N_2H_4 densities; **c** N_2H_4, N_2H_3, H_2NN, N_2H_2, and N_2H densities; and **d** H, N, NH, and NH_2 densities predicted by the kinetic model for 1% NH_3 in Ar, 1 slm, 2.2 W. 1 cm of distance corresponds to between 1.2 and 1.8 ms of gas residence time (Figure S3)

Axially resolved rates for formation and consumption of NH_3, N_2H_4, and N_2 were assessed to identify the reaction steps that contribute most to formation and consumption of these species (Fig. 5). For reactions that do not involve electrons or excited states of atoms/molecules, the net rates ($r_{net} = r_{forward} - r_{reverse}$) are plotted to express the net rates at which the species of interest are formed or consumed.

Figure 5(a) demonstrates that NH_3 dissociation to form NH_2 and H is dominated by electron impact, which is consistent with the inferences of Arakoni et al. [9]. NH_3 is

Fig. 5 Axial profiles of rates of reactions that **a** form and consume NH_3, **b** form and consume N_2H_4, **c** form N_2, **d** form H_2, **e** consume NH_2, and **f** consume H predicted by the kinetic model for 1% NH_3 in Ar, 1 slm, 2.2 W. 1 cm of distance corresponds to between 1.2 and 1.8 ms of gas residence time (Figure S3)

re-formed from the three-body recombination reaction involving NH_2 and H at rates that are on the same order of magnitude as electron impact dissociation of NH_3, indicating that a large fraction of energy deposited into dissociation of NH_3 is wasted to re-form NH_3.

Figure 5(b) shows that N_2H_4 is mainly formed from the three-body recombination reaction involving NH_2 radicals in the plasma and through N_2H_3 disproportionation reactions in the afterglow. N_2H_4 consumption is dominated by H abstraction reactions in and after the plasma. Figure 5(c) shows that the dominant pathway for N_2 formation is through collision-mediated dissociation of N_2H. N_2H is formed from successive dehydrogenation of N_2H_4, N_2H_3, and N_2H_2/H_2NN. N_2 formation from $NH_2 + N$ occurs at a rate over an order of magnitude lower than N_2 formation from N_2H, indicating that N_2 formation mostly occurs through N_2H_x dehydrogenation pathways rather than solely NH_x dehydrogenation pathways. Simulations that eliminate reactions that form/consume N_2H_x species predict NH_3 conversion approximately an order of magnitude lower than those observed in experiments, affirming that the majority of N_2 formation occurs from N_2H_x dehydrogenation pathways (Fig. 6). N_2 consumption occurs primarily by dissociative collisions with Ar^* species, with maximum rates ~ 10^{14} cm^{-3} s^{-1}. Figure 5(d) demonstrates that H_2 is mostly formed from H abstraction from N_2H_x species, demonstrating that the presence of N_2H_x species increases the rate of H_2 formation. H_2 consumption occurs mostly by electron-impact dissociation, with maximum rates ~ 10^{15} cm^{-3} s^{-1}.

Figure 5(e–f) shows the loss pathways of NH_2 and H, the primary products of NH_3 dissociation. At short times, NH_2 mostly reacts to form N_2H_4, but after NH_2 concentration becomes relatively attenuated in comparison to H concentrations over longer (> 300 μs) timescales (Fig. 4(d)), NH_2 reacts with H in three-body recombination reactions at faster rates to re-form NH_3 (Fig. 5(e)). The reaction between NH_2 and H to form NH and H_2 occurs at a rate nearly two orders of magnitude lower than the three-body recombination reaction to re-form NH_3 from NH_2 and H. Figure 5(f) demonstrates that H is consumed by $NH_2 + H + M$ and $N_2H_x + H$ reactions at similar rates.

Discussion

Possible Sources of Error in the Model

Though the kinetic model can accurately describe NH_3 conversion in the plasma, it systematically overestimates N_2H_4 production relative to N_2 production. To assess possible sources of error in the model, a sensitivity analysis was performed.

The kinetic model described in Sect. "Zdplaskin Model". does not include electron-impact reactions involving N_2H_x species, since reaction rate constants for these reactions are unknown/not reported [12]. To probe the role that dissociation of N_2H_x species by nonthermal reactions could have on driving N_2H_x decomposition to N_2, reactions involving dissociation of N_2H_x species by electron impact or by collision with excited states of Ar were included in simulations. For reactions that break an N–N bond in N_2H_x species, rate constants for N_2 dissociation were utilized, and for reactions that break an N–H bond in N_2H_x species, rate constants for NH_3 dissociation were utilized. Results of these

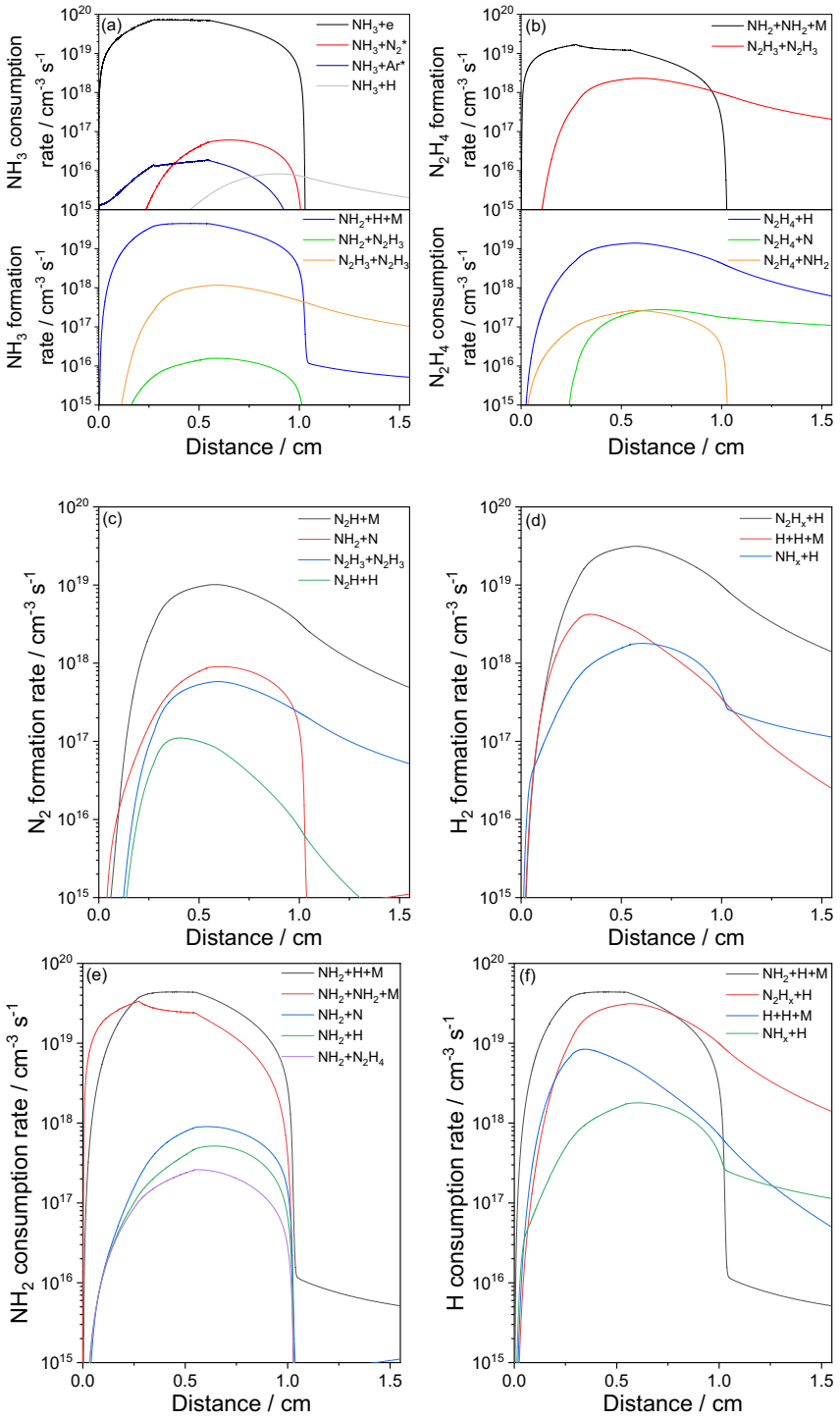
(a)
NH3+e
NH3+N2*
NH3+Ar*
NH3+H
NH2+H+M
NH2+N2H3
N2H3+N2H3
NH3 consumption rate / cm-3 s-1
NH3 formation rate / cm-3 s-1
(b)
NH2+NH2+M
N2H3+N2H3
N2H4+H
N2H4+N
N2H4+NH2
N2H4 formation rate / cm-3 s-1
N2H4 consumption rate / cm-3 s-1
(c)
N2H+M
NH2+N
N2H3+N2H3
N2H+H
N2 formation rate / cm-3 s-1
(d)
N2Hx+H
H+H+M
NHx+H
H2 formation rate / cm-3 s-1
(e)
NH2+H+M
NH2+NH2+M
NH2+N
NH2+H
NH2+N2H4
NH2 consumption rate / cm-3 s-1
(f)
NH2+H+M
N2Hx+H
H+H+M
NHx+H
H consumption rate / cm-3 s-1
Distance / cm

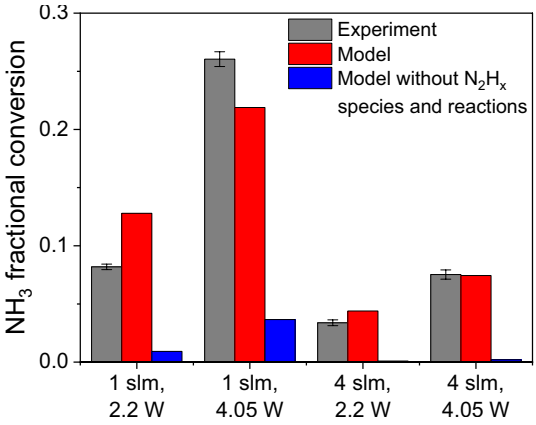

Fig. 6 A comparison of experimentally measured NH_3 conversion and NH_3 conversion predicted by the kinetic model with and without N_2H_x species and reactions. Experimental conditions: 1% NH_3 in Ar, 1–4 slm, 13.8 MHz, 2.2–4.05 plasma-on power, 10 Hz, 50% duty cycle modulation for MBMS measurements. Error bars represent 95% confidence intervals

simulations show that inclusion of these reactions does result in an increase in N_2 selectivity but not to the N_2 selectivity observed in experiments (Fig. 7). N_2 selectivity is still underpredicted by as much as ~ 40%.

The kinetic model could also inaccurately predict N_2 selectivity if the rate coefficients used in the model are inaccurate. A sensitivity analysis was performed in which rate constants for $N_2H_x + H$ reactions (and their associated reverse reactions) were increased by a factor of four (Fig. 8). Results of these simulations show that the model now predicts N_2 selectivity accurately within 7%, although the model now systematically overpredicts NH_3 conversion. These results demonstrate that H abstraction reactions could occur at faster rates than those reported in the model.

Assumptions associated with the plug flow approximation may also contribute to some of the inaccuracies of the simulation results. The model appears to underestimate the electron density and overestimate the electron temperature for reasons discussed in the results section. The plug flow model also assumes that the electron density, electron temperature, gas temperature, and species concentrations are radially uniform at every axial position of the reactor. In the experiments, it is possible that the plasma is constricted, resulting

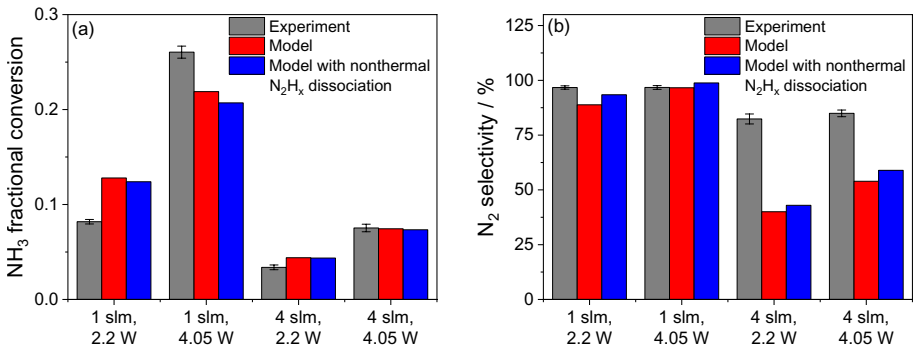

Fig. 7 A comparison of **a** experimentally measured NH_3 conversion and NH_3 conversion predicted by the kinetic model with and without nonthermal N_2H_x dissociation reactions and **b** experimentally measured N_2 selectivity and N_2 selectivity predicted by the kinetic model with and without nonthermal N_2H_x dissociation reactions. Experimental conditions: 1% NH_3 in Ar, 1–4 slm, 13.8 MHz, 2.2–4.05 plasma-on power, 10 Hz, 50% duty cycle modulation for MBMS measurements. Error bars represent 95% confidence intervals

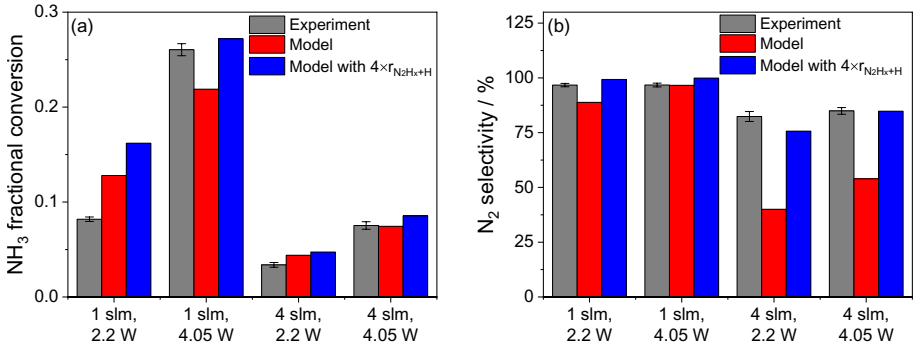

Fig. 8 A comparison of **a** experimentally measured NH_3 conversion and NH_3 conversion predicted by the kinetic model with and without N_2H_x+H reaction rate constants increased 4 × and **b** experimentally measured N_2 selectivity and N_2 selectivity predicted by the kinetic model with and without N_2H_x+H reaction rate constants increased 4 ×. Experimental conditions: 1% NH_3 in Ar, 1–4 slm, 13.8 MHz, 2.2–4.05 plasma-on power, 10 Hz, 50% duty cycle modulation for MBMS measurements. Error bars represent 95% confidence intervals

in regions of the plasma with locally higher gas temperatures and electron densities [38]. Simulations were performed to probe the effect that uneven power deposition may have on dictating the N_2 selectivity and NH_3 conversion. In these simulations, 1/3 of the gas stream is exposed to plasma with 3 × the experimental power density. This stream was then mixed with 2/3 of the unreacted gas stream at the outlet of the reactor to yield a stream with the same SEI as those in experiments. Results of these simulations show that the model now predicts higher N_2 selectivity, especially for the experiments with 4 slm gas flow rates (Fig. 9). Though these simulations are an oversimplification because they do not capture mixing between fluid elements that are exposed to different degrees of power deposition over the length of the reactor and do not consider a continuous gradient in power deposition over the radial coordinate, these simulations demonstrate that uneven power deposition, not considered in the plug-flow model, could contribute to the low N_2H_4 selectivity observed in experiments. Locally higher gas temperatures in a constricted plasma lead

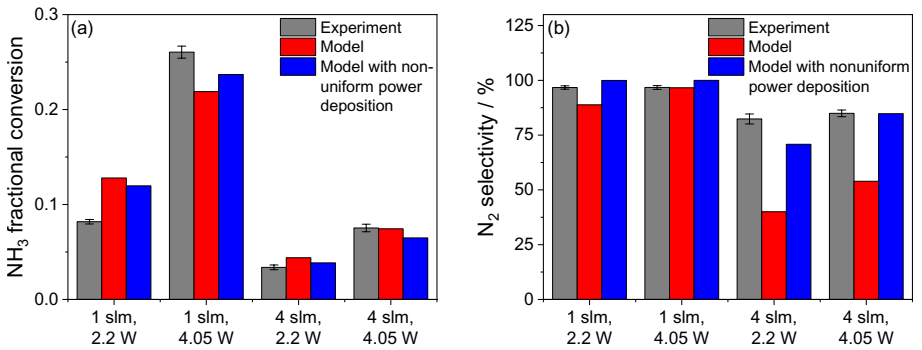

Fig. 9 A comparison of **a** experimentally measured NH_3 conversion and NH_3 conversion predicted by the kinetic model with and without nonuniform power deposition and **b** experimentally measured N_2 selectivity and N_2 selectivity predicted by the kinetic model with and without nonuniform power deposition. Experimental conditions: 1% NH_3 in Ar, 1–4 slm, 13.8 MHz, 2.2–4.05 plasma-on power, 10 Hz, 50% duty cycle modulation for MBMS measurements. Error bars represent 95% confidence intervals

to a greater extent of N_2H_x decomposition, since rate constants for $N_2H_x + H$ reactions increase with gas temperature, while rate constants for the other reactions that consume H ($NH_2 + H + M$, $H + H + M$) are temperature-independent or decrease with temperature (Fig. 5(f), Table S5).

Assessment of the Energy Efficiency of Plasma-Driven NH_3 Decomposition

Experimental data and kinetic modeling results show that NH_3 conversion increases with SEI (Fig. 2(a)). For the 1% NH_3 in Ar plasma investigated in this work, SEI can be converted to energy cost per NH_3 molecule using Eq. 9:

$$\frac{eV}{\text{molecule NH}_3} = 26\left(\frac{\text{J}}{\text{cm}^3}\right) \tag{9}$$

An examination of the slope of the trend in Fig. 2(a) demonstrates ~ 25–50 eV are required to convert one molecule of NH_3. This far exceeds the enthalpy of reaction for NH_3 decomposition ($NH_3 \rightarrow 0.5N_2 + 1.5H_2$, $\Delta H = 46$ kJ (mol NH_3)$^{-1}$ = 0.48 eV (NH_3 molecule)$^{-1}$; $NH_3 \rightarrow 0.5N_2H_4 + 0.5H_2$, $\Delta H = 94$ kJ (mol NH_3)$^{-1}$ = 0.97 eV (NH_3 molecule)$^{-1}$) [3].

Figure 4(a) demonstrates that electron-impact dissociation is the dominant process driving NH_3 decomposition. The energy threshold for this reaction is 5.72 eV [13], indicating that plasma-driven NH_3 decomposition by electron impact dissociation requires 10 × more energy than the enthalpy of reaction for NH_3 decomposition to form N_2 and H_2 [3]. Therefore, 5.72 eV is the lower bound on energy cost for NH_3 decomposition by nonthermal plasma if electron-impact dissociation is the main reaction driving NH_3 dissociation. This value is equivalent to 3.8 eV (molecule H_2 produced)$^{-1}$ if NH_3 is decomposed to N_2 and H_2. As noted by Qiu et al. [6] and Arakoni et al. [9], an energy cost of H_2 production above 2.5 eV (molecule H_2 produced)$^{-1}$ exceeds the amount of energy that can be recovered from H_2 combustion (2.5 eV (molecule H_2 consumed)$^{-1}$) [3]. Therefore, plasma-driven NH_3 decomposition solely from electron impact dissociation has an energy cost too high for H_2 production for energy storage purposes. Plasma-driven processes would need to rely on lower energy processes (excitation-driven or thermal-driven) to drive NH_3 decomposition with a suitable energy cost. If the extra dissipated electron energy beyond 0.48 eV (NH_3 molecule)$^{-1}$ utilized to dissociate NH_3 is effectively utilized to heat the plasma, NH_3 decomposition can be driven by thermal processes in the gas phase [39] or over a catalyst [40, 41].

The 5.72 eV (NH_3 molecule)$^{-1}$ lower bound is still lower than 25–50 eV (NH_3 molecule)$^{-1}$ predicted by experimental measurements and kinetic modeling simulations, so energy dissipation processes are analyzed below to determine where energy is wasted. A comparison between the electron energy deposition into NH_3 dissociation compared to the electron energy deposition into all processes can be analyzed using Eq. 10:

$$\frac{\int_0^{\tau_{end}} E_{\text{NH}_3+\text{e}} r_{\text{NH}_3+\text{e}} dt}{\sum_{\text{I}} \int_0^{\tau_{end}} E_{\text{I}+\text{e}} r_{\text{I}+\text{e}} dt} \tag{10}$$

In Eq. 10, $E_{\text{I+e}}$ is the energy dissipated in a collision between species I and an electron, $r_{\text{I+e}}$ is the rate at which these collisions occur, and τ_{end} is the residence time

associated with the outlet of the reactor (1.55 cm). For the process condition analyzed in Figs. 4–5, this fraction is equal to 0.93, indicating that the plasma very efficiently directs electron energy towards NH_3 dissociation in comparison to elastic collisions, ionization, excitation, and other dissociation processes.

To assess whether the products of NH_3 electron impact dissociation are effectively converted to desired products, the fraction of NH_2 molecules that are converted to N_2H_4 vs NH_2 converted to N_2H_4 or NH_3 can be analyzed using Eq. 11:

$$\frac{\#\,NH_2 \text{ to } N_2H_4}{\#\,NH_2 \text{ converted}} = \frac{\int_0^{\tau_{end}} 2r_{NH_2+NH_2+M}d\tau}{\int_0^{\tau_{end}} r_{NH_2+H+M}d\tau + \int_0^{\tau_{end}} 2r_{NH_2+NH_2+M}d\tau} \tag{11}$$

For the process condition analyzed in Figs. 3 and 4, this fraction is equal to 0.41, indicating that more than half of the NH_2 molecules formed from electron-impact dissociation of NH_3 are re-converted to NH_3. Limiting the extent to which NH_3 is re-formed from three-body collisions between NH_2 and H is critical to improving the utilization of NH_3 dissociation products for N_2/H_2 formation. To do this, process conditions must be chosen that increase the rates at which NH_2 and H react to form N_2H_4 or N_2 products vs recombine to form NH_3. The ratio of the rate of N_2H_4 formation vs NH_3 formation by three-body recombination takes the form of Eq. 12:

$$\frac{r_{NH_2+NH_2+M}}{r_{NH_2+H+M}} = \frac{k_{NH_2+NH_2+M}c_{NH_2}c_{NH_2}c_M}{k_{NH_2+H+M}c_{NH_2}c_Hc_M} = \frac{2.1\cdot 10^{10}}{T_g^{\,3.41}}\frac{c_{NH_2}}{c_H} \tag{12}$$

An analysis of this ratio shows that the branching ratio between N_2H_4 formation and NH_3 formation is not easily manipulated by varying process conditions. Lower temperature would favor N_2H_4 formation over NH_3 formation, although as the gas temperature increases and NH_2 concentrations become relatively lower than H concentrations as observed in Fig. 4, NH_2 consumption to form NH_3 becomes more pronounced.

Although not a dominant reaction in these experiments, the reaction between NH_2 and H to form NH and H_2 can consume NH_2 and H to eventually form N_2 and H_2 instead of re-forming NH_3. The ratio of the rates of these processes takes the form of Eq. 13:

$$\frac{r_{NH_2+H}}{r_{NH_2+H+M}} = \frac{k_{NH_2+H}c_{NH_2}c_H}{k_{NH_2+H+M}c_{NH_2}c_Hc_M} = \frac{36\cdot\exp(-1835/T_g)RT_g}{p} \tag{13}$$

This ratio is dependent on both gas temperature and pressure, with higher temperatures and lower pressures favoring NH_2+H conversion to NH and H_2 instead of NH_3. At atmospheric pressure, 0.1 bar, and 0.01 bar, the ratio of these reaction rates becomes greater than 1 at 1330 K, 630 K, and 386 K, respectively. Operating at lower pressure could thus improve energy efficiency by mitigating re-formation of NH_3 by three-body recombination reactions involving NH_2 and H. Additionally, the mechanism for N_2 formation from NH_3 decomposition could shift from the N_2H_x formation/decomposition pathway exhibited at atmospheric pressure to a NH_x decomposition pathway as rates of three body recombination reactions between two NH_2 molecules to form N_2H_4 become relatively attenuated at reduced pressures. As a result, operating at lower pressure could also improve the selectivity towards N_2 formation, even at lower temperatures and NH_3 conversions.

Conclusions

Reaction pathways and energy consumption for NH_3 decomposition in an RF-driven atmospheric pressure plasma jet are assessed using a combination of molecular beam mass spectrometry and zero-dimensional kinetic modeling. MBMS measurements show that N_2 and N_2H_4 are the main products of NH_3 decomposition and that the extent of NH_3 conversion and the selectivity towards N_2 formation scales monotonically with the specific energy input into the plasma. Kinetic modeling shows that N_2H_4 is an intermediate in N_2 formation from NH_3 decomposition and rates of N_2H_4 decomposition increase with gas temperature, which explains why N_2H_4 selectivity is relatively higher at lower NH_3 conversion and lower gas temperatures. Though the kinetic model systematically underestimates N_2 selectivity at low specific energy inputs, a sensitivity analysis demonstrates that this underestimation can be explained by the underestimation of rate constants for reactions that consume N_2H_x species in the model and/or the inaccurate assumption of radially uniform power deposition, gas temperature, and species concentrations associated with the plug-flow approximation of the model.

An analysis of the energy deposition processes shows that NH_3 dissociation is dominated by electron-impact dissociation in this study, which has an energy threshold of 5.72 eV. Therefore, 5.72 eV is the lower bound on the energy cost for NH_3 decomposition if electron-impact dissociation is the dominant process for NH_3 dissociation in plasma. This energy cost is ~ 10 × higher than the enthalpy of NH_3 decomposition to N_2 and H_2 (0.48 eV (molecule NH_3 consumed) $^{-1}$). This value is also higher than the energy that can be derived from H_2 combustion (2.5 eV (molecule H_2 consumed)$^{-1}$), indicating that plasma-driven NH_3 decomposition using electron impact dissociation inherently has an energy cost too high for energy storage applications. NH_3 re-formation from three-body collisions between NH_2 and H, the primary products of NH_3 dissociation, further lowers the energy efficiency of the process. To produce H_2 from plasma-driven NH_3 decomposition with an energy cost below 2.5 eV (molecule H_2 produced)$^{-1}$, plasma-driven NH_3 decomposition would need to utilize processes other than electron-impact dissociation to induce NH_3 dissociation (excitation-driven or thermal-driven) and would need to limit energy loss from NH_3 re-forming reactions.

Supplementary Information The online version contains supplementary material available at https://doi.org/10.1007/s11090-024-10501-8.

Author Contributions Brian N. Bayer: Conceptualization, Data curation, Formal analysis, Investigation, Methodology, Project administration, Writing—original draft, Writing—review & editing. Aditya Bhan: Conceptualization, Funding acquisition, Methodology, Project administration, Resources, Supervision, Writing—review & editing. Peter J. Bruggeman: Conceptualization, Funding acquisition, Methodology, Project administration, Resources, Supervision, Writing—review & editing.

Funding This material is based upon work supported by the U.S. Department of Energy, Office of Science, Office of Fusion Energy Sciences General Plasma Science program under Award Number DE-SC0020232. The work heavily relied on equipment and methods developed within project DE-SC0001939. The authors also acknowledge partial support from the National Science Foundation under Award Number NSF-CBET 2234270.

Data Availability All data presented in this work will be made available upon request to the corresponding author.

Declarations

Conflict of interest The authors have no competing interests to declare that are relevant to the content of this article.

References

1. MacFarlane DR, Cherepanov PV, Choi J, Suryanto BHR, Hodgetts RY, Bakker JM, Ferrero Vallana FM, Simonov AN (2020) A roadmap to the ammonia economy. Joule 4:1186–1205. https://doi.org/10.1016/j.joule.2020.04.004
2. Valera-Medina A, Xiao H, Owen-Jones M, David WIF, Bowen PJ (2018) Ammonia for power. Prog Energy Combust Sci 69:63–102. https://doi.org/10.1016/j.pecs.2018.07.001
3. NIST (2010) Standard Reference Database 69: NIST Chemistry WebBook; National Institute of Standards and Technology, (n.d.)
4. Benés M, Pozo G, Abián M, Millera Á, Bilbao R, Alzueta MU (2021) Experimental study of the pyrolysis of NH_3 under flow reactor conditions. Energy Fuels 35:7193–7200. https://doi.org/10.1021/acs.energyfuels.0c03387
5. Caballero LC, Thornburg NE, Nigra MM (2022) Catalytic ammonia reforming: alternative routes to net-zero-carbon hydrogen and fuel. Chem Sci 13:12945–12956. https://doi.org/10.1039/D2SC04672E
6. Qiu H, Martus K, Lee WY, Becker K (2004) Hydrogen generation in a microhollow cathode discharge in high-pressure ammonia–argon gas mixtures. Int J Mass Spectrom 233:19–24. https://doi.org/10.1016/j.ijms.2003.08.017
7. Gao Y, Zhou M, Hu E, Zhao Y, Yin G, Huang Z (2024) Hydrogen generation by dielectric barrier discharge plasma assisted ammonia decomposition. Energy Convers Manag 306:118271. https://doi.org/10.1016/j.enconman.2024.118271
8. Ruiz-Martín M, Marín-Meana S, Megías-Sánchez A, Oliva-Ramírez M, Cotrino J, González-Elipe AR, Gómez-Ramírez A (2023) H_2 Production from NH_3 in a $BaTiO_3$ Moderated ferroelectric packed-bed plasma reactor. Plasma Chem Plasma Process 43:2093–2110. https://doi.org/10.1007/s11090-023-10427-7
9. Arakoni RA, Bhoj AN, Kushner MJ (2007) H_2 generation in Ar/NH_3 microdischarges. J Phys D: Appl Phys 40:2476. https://doi.org/10.1088/0022-3727/40/8/010
10. Fateev A, Leipold F, Kusano Y, Stenum B, Tsakadze E, Bindslev H (2005) Plasma chemistry in an atmospheric pressure Ar/NH_3 dielectric barrier discharge. Plasma Process Polym 2:193–200. https://doi.org/10.1002/ppap.200400051
11. Troyan JE (1953) Properties, production, and uses of hydrazine. Ind Eng Chem 45:2608–2612. https://doi.org/10.1021/ie50528a020
12. Bang S, Snoeckx R, Cha MS (2023) Kinetic study for plasma assisted cracking of NH_3: approaches and challenges. J Phys Chem A 127:1271–1282. https://doi.org/10.1021/acs.jpca.2c06919
13. Hayashi database (2024) (n.d.). www.lxcat.net. Accessed 4 June 2024
14. Kondeti VSSK, Gangal U, Yatom S, Bruggeman PJ (2017) Ag^+ reduction and silver nanoparticle synthesis at the plasma–liquid interface by an RF driven atmospheric pressure plasma jet: mechanisms and the effect of surfactant. J Vac Sci Technol, A 35:061302. https://doi.org/10.1116/1.4995374
15. Hofmann S, van Gessel AFH, Verreycken T, Bruggeman P (2011) Power dissipation, gas temperatures and electron densities of cold atmospheric pressure helium and argon RF plasma jets. Plasma Sources Sci Technol 20:065010. https://doi.org/10.1088/0963-0252/20/6/065010
16. Jiang J, Luo Y, Moldgy A, Aranda Gonzalvo Y, Bruggeman PJ (2020) Absolute spatially and time-resolved O, O_3, and air densities in the effluent of a modulated RF-driven atmospheric pressure plasma jet obtained by molecular beam mass spectrometry. Plasma Process Polym 17:1900163. https://doi.org/10.1002/ppap.201900163
17. Bayer BN, Bruggeman PJ, Bhan A (2023) Species, pathways, and timescales for NH_3 formation by low-temperature atmospheric pressure plasma catalysis. ACS Catal 13:2619–2630. https://doi.org/10.1021/acscatal.2c05492
18. Benedikt J, Hecimovic A, Ellerweg D, von Keudell A (2012) Quadrupole mass spectrometry of reactive plasmas. J Phys D: Appl Phys 45:403001. https://doi.org/10.1088/0022-3727/45/40/403001
19. Singh H, Coburn JW, Graves DB (2000) Appearance potential mass spectrometry: discrimination of dissociative ionization products. J Vac Sci Technol, A 18:299–305. https://doi.org/10.1116/1.582183
20. Jiang J, Richards C, Adamovich I, Bruggeman PJ (2022) Molecular beam mass spectrometry measurements of vibrationally excited N_2 in the effluent of an atmospheric plasma jet: a comparison with a state-to-state kinetic model. Plasma Sources Sci Technol 31:10LT03. https://doi.org/10.1088/1361-6595/ac954c
21. Bayer BN, Raskar S, Adamovich IV, Bruggeman PJ, Bhan A (2023) Availability and reactivity of N_2(v) for NH_3 synthesis by plasma catalysis. Plasma Sources Sci Technol 32:125005. https://doi.org/10.1088/1361-6595/ad10f0
22. Jiang J, Bruggeman PJ (2021) Tuning plasma parameters to control reactive species fluxes to substrates in the context of plasma catalysis. J Phys D: Appl Phys 54:214005. https://doi.org/10.1088/1361-6463/abe89a

23. Pancheshni S, Eismann B, Hagelaar GJM, Pitchford LC (2008) Computer code ZDPlasKin. http://www.zdplaskin.laplace.univ-tlse.fr
24. Hagelaar GJM, Pitchford LC (2005) Solving the Boltzmann equation to obtain electron transport coefficients and rate coefficients for fluid models. Plasma Sources Sci Technol 14:722. https://doi.org/10.1088/0963-0252/14/4/011
25. Jiang J, Kondeti VSSK, Nayak G, Bruggeman PJ (2022) Experimental and modeling studies of the plasma chemistry in a humid Ar radiofrequency atmospheric pressure plasma jet. J Phys D: Appl Phys 55:225206. https://doi.org/10.1088/1361-6463/ac570a
26. Bayer BN, Bruggeman PJ, Bhan A (2024) NO formation by N_2/O_2 plasma catalysis: the impact of surface reactions, gas-phase reactions, and mass transport. Chem Eng J 482:149041. https://doi.org/10.1016/j.cej.2024.149041
27. Lisbon database (2024) (n.d.). www.lxcat.net. Accessed 4 June 2024
28. Gaens WV, Bogaerts A (2013) Kinetic modelling for an atmospheric pressure argon plasma jet in humid air. J Phys D: Appl Phys 46:275201. https://doi.org/10.1088/0022-3727/46/27/275201
29. Alturaifi SA, Mathieu O, Petersen EL (2022) An experimental and modeling study of ammonia pyrolysis. Combust Flame 235:111694. https://doi.org/10.1016/j.combustflame.2021.111694
30. Gordiets B, Ferreira CM, Pinheiro MJ, Ricard A (1998) Self-consistent kinetic model of low-pressure - flowing discharges: I. volume processes. Plasma Sources Sci Technol 7:363–378. https://doi.org/10.1088/0963-0252/7/3/015
31. Pagsberg PB, Eriksen J, Christensen HC (1979) Pulse radiolysis of gaseous ammonia-oxygen mixtures. J Phys Chem 83:582–590. https://doi.org/10.1021/j100468a006
32. Zheng J, Rocha RJ, Pelegrini M, Ferrão LFA, Carvalho EFV, Roberto-Neto O, Machado FBC, Truhlar DG (2012) A product branching ratio controlled by vibrational adiabaticity and variational effects: Kinetics of the H + trans-N_2H_2 reactions. J Chem Phys 136:184310. https://doi.org/10.1063/1.4707734
33. Altinay G, Macdonald RG (2015) Determination of the rate constants for the $NH_2(X^2B_1)$ + $NH_2(X^2B_1)$ and $NH_2(X^2B_1)$ + H recombination reactions in N_2 as a function of temperature and pressure. J Phys Chem A 119:7593–7610. https://doi.org/10.1021/acs.jpca.5b00917
34. Goos E, Burcat A, Ruscic B (2006) Extended third millenium ideal gas and condensed phase thermochemical database for combustion with updates from active thermochemical tables. http://garfield.chem.elte.hu/Burcat/THERM.DAT (accessed June 6, 2024)
35. Andersen JA, van'tVeerChristensenØstbergBogaertsJensen KJMMAAD (2023) Ammonia decomposition in a dielectric barrier discharge plasma: insights from experiments and kinetic modeling. Chem Eng Sci 271:118550 https://doi.org/10.1016/j.ces.2023.118550
36. van Gessel B, Brandenburg R, Bruggeman P (2013) Electron properties and air mixing in radio frequency driven argon plasma jets at atmospheric pressure. Appl Phys Lett 103:064103. https://doi.org/10.1063/1.4817936
37. Jiang J, Bruggeman PJ (2021) Absolute ion density measurements in the afterglow of a radiofrequency atmospheric pressure plasma jet. J Phys D: Appl Phys 54:15LT01. https://doi.org/10.1088/1361-6463/abdc91
38. von Keudell A, der Gathen VS (2017) Foundations of low-temperature plasma physics—an introduction. Plasma Sources Sci Technol 26:113001. https://doi.org/10.1088/1361-6595/aa8d4c
39. Bruggeman PJ, Iza F, Brandenburg R (2017) Foundations of atmospheric pressure non-equilibrium plasmas. Plasma Sources Sci Technol 26:123002. https://doi.org/10.1088/1361-6595/aa97af
40. Hsu DD, Graves DB (2005) Microhollow Cathode Discharge Reactor Chemistry. Plasma Chem Plasma Process 25:1–17. https://doi.org/10.1007/s11090-004-8831-8
41. Wang L, Zhao Y, Liu C, Gong W, Guo H (2013) Plasma driven ammonia decomposition on a Fe-catalyst: eliminating surface nitrogen poisoning. Chem Commun 49:3787–3789. https://doi.org/10.1039/C3CC41301B
42. Wang N, Otor HO, Rivera-Castro G, Hicks JC (2024) Plasma Catalysis for Hydrogen Production: A Bright Future for Decarbonization. ACS Catal 14(9):6749–6798. https://doi.org/10.1021/acscatal.3c05434